RSC Advances

PAPER

View Article Online
View Journal | View Issue

Cite this: *RSC Adv.*, 2021, **11**, 9353

A template-directed synthesis of metal–organic framework (MOF-74) ultrathin nanosheets for oxygen reduction electrocatalysis†

Rui Fan, Ning Kang, Yuzhen Li and Lizhen Gao*

Received 25th November 2020
Accepted 7th February 2021

DOI: 10.1039/d0ra09973b

rsc.li/rsc-advances

Metal–organic frameworks (MOFs) have received wide attention for their promising applications in numerous fields due to their tailorable structure, metal centers and porosity. However, the low mass permeability, poor conductivity and blockage of active metal centers severely restrict the utilization of MOF systems in electrocatalysis. Two-dimensionalization can endow MOF materials extra unsaturated metal centers and enhanced electron-transfer ability, and could be an effective strategy to achieve high-performance MOF-based electrocatalysts. Herein, Ni-MOF-74 nanosheets are synthesized using layered double hydroxide (LDH) as a template to directly grow ultrathin structures. Benefiting from the two-dimensional structure, Ni-MOF-74 nanosheets with carbon substrate exhibit an enhanced ORR electrocatalytic property with positive half-wave potential (+0.83 V *vs.* RHE), a large current density (3.9 mA cm^{-2}), four-electron selectivity and a promising long-term durability.

1. Introduction

Metal–organic frameworks (MOFs) are a class of crystalline materials, the network built up from metal atoms and numerous organic ligands *via* coordination bonds,[1] have captured widespread interest and achieved the explosive development over the past two decades.[2,3] The crystalline nature, tailorable structure, and porosity as well as ultrahigh surface area give MOFs great potential for various applications, such as gas storage, separation, catalysis, sensors, biomedicine and electrochemical applications.[4–10] Recently, MOF materials have developed as electrocatalysts for renewable energy storage and conversion, mainly consisting of oxygen reduction reaction (ORR)[11–13] and electrochemical water splitting (OER/HER).[14–16] In the MOF-based electrocatalysts, the metal nodes (Fe, Co, Ni, *etc.*) in MOFs can be served as non-noble metal catalytic active sites, and the tailorable structure of MOFs also brings several merits for these electrocatalytic systems, such as large surface area and tunable pore size.[17,18] However, to date, reported MOF systems still suffer from low mass permeability, poor conductivity and blockage of active metal centers by organic ligands, dramatically limiting their utilization as electrocatalysts. Based on those drawbacks of MOFs, further modification of the structure is required for developing the electrocatalytic activities of MOFs.

Two-dimensionalization could be an effective strategy to achieve high-performance MOF-based electrocatalysts.[19] Compared with traditional bulk materials, there are three unique advantages to put two-dimensional (2D) nanosheets into use: (1) the high percentage of exposed surfaces can offer more unsaturated metal active sites to enhance catalytic activity; (2) the nanometer thicknesses will accelerate mass transport and electron transfer; and (3) the unique open structure makes more interior atoms exposed as accessible active sites.[20–22] Thus, ultrathin MOF nanosheets could be an ideal model system, which not only could be designed as high-performance electrocatalysts, but have numerous promising applications in catalysis, sensors and supercapacitors and so on.[19] Unfortunately, due to the intrinsic isotropic chemically bond, it is not easy to only downsize a dimension of MOFs with a 3D topological structure,[23] and there have been few reports on preparing 2D MOF nanosheets for now.[24–26] Therefore, in order to control the 2D anisotropic growth of MOF materials, the synthetic process must break the thermodynamic equilibrium state and the controllability of kinetics must be artificially introduced.

As one of the most important MOFs, MOF-74 (M = Co, Ni), with high density and open unsaturated coordination sites, has been widely studied since it was first reported in 2005.[27] MOF-74 has a 3D topological structure with hexagonal channels, with diameters about 11 Å; each metal atom of MOFs has coordinated with five oxygen atoms on carboxyl and hydroxyl of 2,5-dihydroxyterephthalic acid molecules (DHTA) to form a quasi-square pyramidal structure; the sixth coordination site of the metal atom is occupied by an absorbed guest molecule, which is easy to remove to expose an unsaturated metal site.[28] Owing to

College of Environmental Science and Engineering, Taiyuan University of Technology, Taiyuan, China. E-mail: lzgao1@yahoo.com

† Electronic supplementary information (ESI) available. See DOI: 10.1039/d0ra09973b

the 3D porous structure and unsaturated metal sites, MOF-74 has wide applications in gas storage, separation and adsorption.[29–32] However, in electrocatalytic systems, MOF-74 is used as a precursor to prepare carbon and metal-based catalysts,[33,34] which is hard to realize the deserved value of MOF-74 in electrocatalysis. Combined with the 2D structure, ultrathin MOF-74 nanosheets exhibit more unsaturated transition metal active sites, and a better capability of electronic transfer because of the nanometer thicknesses. Thus, two-dimensionalization can substantially enhance the electrocatalytic properties of MOF-74, and exploring effective synthetic methods of MOF-74 ultrathin nanosheets is necessary.

Herein, in order to realize the two-dimensionalization of MOF-74, we propose a novel strategy using layered double hydroxide (LDH) as a template to directly grow ultrathin structure. Owing to the structure memory and absorbability to anion,[35,36] the interlayer of LDH is a micro-reactor to provide steric hindrance, which is propitious to limit the vertical dimension growth of MOF-74. As a result, Ni-MOF-74 ultrathin nanosheets are achieved in the interlayer of LDH. Benefiting from the ultrathin structure, Ni-MOF-74 nanosheets exhibit an enhanced ORR catalytic property in alkaline with positive half-wave potential (+0.74 V *vs.* RHE). After adding acetylene black, the electrocatalytic activities of Ni-MOF-74 nanosheets achieved further improvements, and the half-wave potential and current density arrived at +0.83 V (*vs.* RHE) and 3.9 mA cm^{-2}, respectively. Based on the enhanced electrocatalytic performance, ultrathin Ni-MOF-74 nanosheets have great potential as the electrode materials for fuel cells and metal–air batteries, and our findings could inspire the further exploration of ultrathin structures in MOF systems.

2. Experimental details

2.1 Material

2,5-Dihydroxyterephthalic acid (DHTA) and nickel acetate ($Ni(CH_3COO)\cdot 4H_2O$) were purchased from Aladdin Company. Acetylene Black (AB) was purchased from Alfa Aesar. Magnesium nitrate hexahydrate ($Mg(NO_3)_2\cdot 6H_2O$), aluminum nitrate nonahydrate ($Al(NO_3)_3\cdot 9H_2O$), sodium carbonate (Na_2CO_3), sodium hydroxide were purchased from Sinopharm Chemical Reagent. All reagents needed no further purification. The Pt/C catalyst (20 wt% Pt on Vulcan XC72R carbon) was purchased from Johnson Matthey Corporation. Other chemicals were purchased from Beijing Chemical Reagent Company.

2.2 Synthesis of the MgAl-LDH template

7.69 g of $Mg(NO_3)_2\cdot 6H_2O$ and 3.75 g of $Al(NO_3)_3\cdot 9H_2O$ were dissolved in 50 mL deionized water (A solution), and 9.54 g of Na_2CO_3 was dissolved in 100 mL deionized water (B solution), and then solution A was dropwise added into solution B slowly. The pH value was adjusted to 11 using a NaOH solution (1.5 mol L^{-1}). The mixture was subsequently transferred into a 100 mL Teflon-lined stainless-steel autoclave and incubated in an oven at 120 °C for 24 h and the autoclave was cooled to room temperature. The product was filtered under vacuum, washed by deionized water, and heated to 80 °C until completely drying. Then, the LDO template was synthesized by a one-step pyrolytic approach in air. Briefly, the as-prepared MgAl-LDH was put into a crucible. The crucible was heated to 500 °C at a rate of 4 °C min^{-1} in a muffle furnace, maintained for 180 min, and then cooled to room temperature. The as-prepared LDO template was bright white in color, which was ground into powder for further use.

2.3 Synthesis of Ni-MOF-74

2.3.1 Synthesis of bulk Ni-MOF-74. 0.52 g of DHTA was dissolved in a 40 mL mixed solvent of deionized water and ethanol (v/v = 1/1), and then 20 mL nickel acetate solution (1.30 g) was added to the mixed solution. The mixed solution was refluxed for 6 h and cooled to room temperature, and the obtained green powder is the bulk Ni-MOF-74 sample.

2.3.2 Synthesis of Ni-MOF-74 nanosheets. 0.52 g of DHTA was dissolved in a 40 mL mixed solvent of deionized water and ethanol (v/v = 1/1), and then 2 g of LDO template was added to the mixed solution and stirred overnight. The solid was obtained *via* vacuum filtration to remove unabsorbed ligand molecule and re-dispersed into the 40 mL mix solvent of deionized water and ethanol, and 15 mL nickel acetate solution (0.65 g) was added into the mixed solution and pH was adjusted to 6. Further, the mixed solution was refluxed overnight to obtain an Ni-MOF-74/LDH intercalated compound. In this study, a weak acid was used to remove the LDH template, and the obtained Ni-MOF-74/LDH intercalated compound was put into the weak HCl solution (pH = 3) and stirred 2 h; this procedure was repeated numerous times until the pH of the dispersion liquid remained 3. Dialysis was performed to remove the unexpected ions to achieve pure Ni-MOF-74 nanosheets. Finally, the product of Ni-MOF-74 nanosheets was froze dried to obtain green powder, and its weight is about 200 mg.

2.3.3 Synthesis of Ni-MOF-74/AB. Similar to the synthetic strategy of Ni-MOF-74 nanosheets, in the template removal process, equivalent acetylene black was added into the dispersion liquid of Ni-MOF-74 nanosheets to prepare a hybrid system, denoted as Ni-MOF-74/AB.

2.4 Characterization

2.4.1 Physical characterization. The transmission electron microscopy (TEM) images were recorded on Tecnai G2 F20. The scanning electron microscopy (SEM) measurements were performed on a HITACHI SU8220 instrument. The X-ray powder diffraction (XRD) patterns were measured in reflection mode (Cu KR radiation) on Bruker D8 Advance. X-ray Photoelectron Spectroscopy (XPS) spectra were recorded using a Kratos Analytical AXIS ULTRA spectrometer with a mono X-ray source Al Kα excitation (1486.6 eV).

2.4.2 Electrochemical measurements. The electrochemical tests were conducted using CHI 660B (Shanghai, China) with a typical three-electrode cell. A graphite rod was used as the counter electrode and a saturated calomel electrode (SCE) as the reference electrode. The working electrode was prepared by applying the catalyst ink onto a pre-polished glassy carbon

electrode (GCE) and a GC rotating disk electrode (RDE). Briefly, the sample was dispersed in the mixed solvent of ultrapure water and DMF (v/v = 1 : 1) under ultrasonication for 15 min to form a uniform sample ink (4 mg mL^{-1}). A total of 10 μL well-dispersed sample ink was applied onto the clean surface of the electrode (3 mm in diameter). After drying at room temperature, 5 μL of Nafion solution in ethanol (0.5 wt%) was dropped onto the surface of the catalyst layer to form a thin protective film. The addition of a small amount of Nafion could effectively improve the dispersion of the catalyst suspension and enhance its binding onto the GCE surface. The as-prepared electrodes were dried at room temperature for overnight. Prior to the experiments, the electrolyte solutions were purged with O_2 for 30 min. Also, the headspace of the electrochemical cell was continuously purged with O_2 during the measurements. All the experiments were conducted at ambient conditions. The Koutecky–Levich (K–L) plots were analyzed at different electrode potentials. Based on the K–L equation, the electron transfer number (n) is calculated from the slope of the K–L plot:

$$\frac{1}{J} = \frac{1}{J_K} + \frac{1}{B\omega^{1/2}}$$

$$B = 0.2nFC_0(D_0)^{2/3}(\nu)^{-1/6}$$

in which, J is the measured current density, J_K is the kinetic limiting current density, ω is the electrode rotating rate, n is the electron transfer number, F is the Faraday constant (F = 96 485C mol^{-1}), C_0 is the bulk concentration of O_2 ($C_0 = 1.2 \times 10^{-6}$ mol cm^{-3}), D_0 is the diffusion coefficient of O_2 in 0.1 M KOH ($D_0 = 1.9 \times 10^{-5}$ cm^2 s^{-1}), and ν is the kinetic viscosity (ν = 0.01 cm^2 s^{-1}). All the potentials reported were referenced to a reversible hydrogen electrode (RHE) by adding a value of (0.2438 + 0.059pH) V.

3. Results and discussion

The growth of ultrathin Ni-MOF-74 nanosheets is directed by the LDH template *via* a two-step adsorption–complexation process, as shown in Fig. 1. Owing to electrostatic attraction, DHTA molecules adsorbed and anchored into the interlayer of LDH to form a uniform sandwich structure. Then, nickel ions permeated into the interlayer of LDH and the complex reaction occurred with the adsorbed DHTA molecules to form the MOF-74 structure in the interlayer of LDH *via* refluxing. Finally, a weak acid was used to remove the LDH template *via* neutralization reaction, leading to the generation of pure Ni-MOF-74 ultrathin nanosheets. Thus, in this synthetic process, the LDH template plays the most important role as a 2D micro-reactor to regulate the growth of Ni-MOF-74 and achieve its two-dimensionalization.

To confirm this hypothesis, the X-ray powder diffraction (XRD) and scanning electron microscopy (SEM) were carried out to investigate the structure of the LDH template. Fig. S1† shows the XRD pattern of LDH, and the diffraction peaks can be attributed to the crystal structure of hydrotalcite (ICDD no. 00-014-0191). The diffraction peak at 11.64° belongs to the (003) crystalline phase (vertical to plane) of LDH, indicating the calculated interlayer spacing of LDH with intercalated CO_3^{2-} (see ESI†) is closed to 7.62 Å. The microstructure of LDH was characterized *via* scanning electron microscope (SEM). The image is shown in Fig. S2,† which shows a typical morphology for the LDH template: a homogeneous hexagonal sheet-like structure with the average size of about 300 nm. After, the heat-treatment process, the diffraction peak (003) completely disappeared, which illustrates the layered structure of LDH has collapsed to form a bimetal oxide (LDO). Owing to the structure memory of LDH, treated by the adsorption process of the DHTA molecule, the diffraction peaks are returned back to hydrotalcite, manifesting that LDO has already restored to the layered structure of LDH. Besides, compared to the 11.6° of hydrotalcite, the (003) diffraction peak of DHTA/LDH is transferred to 10.96°, which indicates that DHTA molecules have entered into the interlayer of LDH to form intercalated compounds, leading a larger interlayer spacing of LDH (8.09 Å) than that of hydrotalcite.[37] Consequently, LDH can be used as an ideal micro-reactor to synthesize Ni-MOF-74 ultrathin nanosheets.

X-ray diffraction (XRD) was used to investigate the crystalline structure of Ni-MOF-74 ultrathin nanosheets. The XRD pattern of the as-prepared Ni-MOF-74 nanosheets in Fig. 2a reveals the peaks at 6.84°, 11.88°, 24.92°, 33.74°, and 36.34°, which are in good agreement with bulk Ni-MOF-74.[38] Clearly, the two-dimensionalization barely effects the crystal structure of Ni-MOF-74, which still maintains a good crystallization. The scanning electron microscopy (SEM) measurement is carried out to further investigate the morphology of the as-prepared Ni-

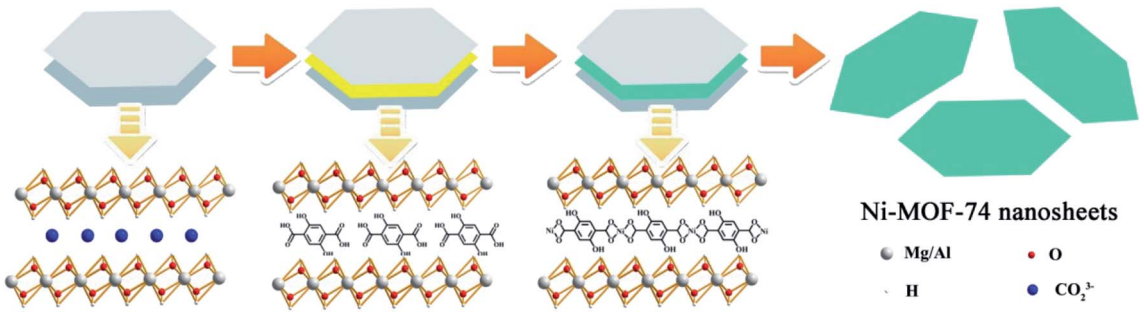

Fig. 1 Schematic of the synthetic protocol for Ni-MOF-74 ultrathin nanosheets.

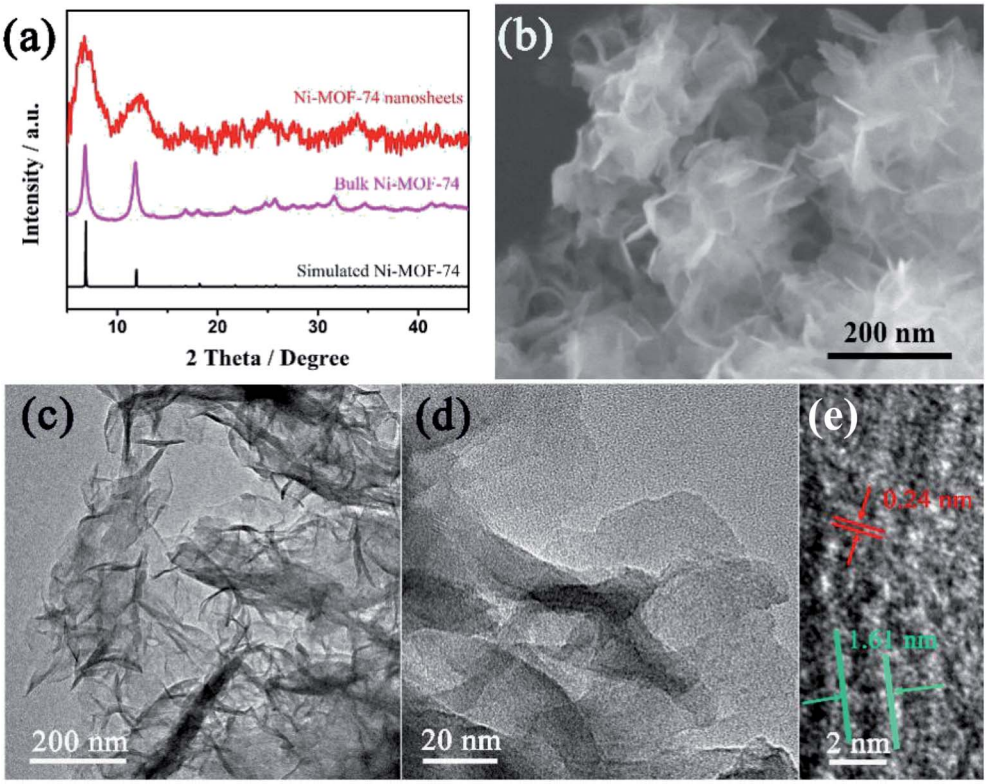

Fig. 2 (a) XRD patterns of bulk Ni-MOF-74, Ni-MOF-74 nanosheets and simulated Ni-MOF-74 nanosheets. (b) The SEM image, (c) and (d) TEM, (e) high resolution TEM images of Ni-MOF-74 nanosheets.

MOF-74 sample. In Fig. 2b and S3,† the Ni-MOF-74 sample exhibits a crinkled and smooth layered structure, comprising of continuous but entangled ultrathin nanosheets, indicating that the LDH template has raised the function of steric hindrance and effectively limited the vertical growth of Ni-MOF-74. The Ni-MOF-74 nanosheets interconnect to constitute an anomalous 3D porous morphology. The unique morphology of Ni-MOF-74 nanosheets could be attributed to the sluggish template removal process. In this study, a weak acid is used to slowly remove the LDH template, leading to the partial interaction of Ni-MOF-74 nanosheets to form an extra porous structure. The hierarchical porous structure can not only endow Ni-MOF-74 with additional surface area and expose more active centers, but also facilitate small molecule diffusion, which can enhance the electrocatalytic activities of Ni-MOF-74 nanosheets for ORR. Besides, the transmission electron microscopy (TEM) images in Fig. 2d and e also confirm the 2D structure of the Ni-MOF-74 sample. Similar to the result of the SEM analysis, the microstructure of the Ni-MOF-74 nanosheets shows a typical homogeneous and sheet-like morphology without any impurity particles, indicating that LDH has been totally removed in the acid washing process. The high resolution TEM image in Fig. 2e reveals that Ni-MOF-74 nanosheets possess a few-layered structure with high crystallinity, and the interlayer spacing is about 1.61 nm and the lattice spacing is 0.24 nm.

X-ray photoelectron spectroscopy (XPS) measurement and energy dispersive spectroscopy (EDS) elemental mapping were carried out to probe the elemental composition of Ni-MOF-74 ultrathin nanosheets. In Fig. 3a, the XPS spectrum shows that the Ni-MOF-74 nanosheets consisted of carbon, oxygen and nickel, and the element contents are 54%, 35% and 11%, respectively. After fitting by the function of Gaussian, the high-resolution XPS spectrum of C 1s in Fig. 3b, which exhibits two subpeaks at 282.4 and 285.5 eV, separately assigned to the C=C and C–O binding energies of the DHTA molecule. For the XPS spectrum of Ni 2p, two characteristic peaks at 853.8 eV (Ni $2p_{3/2}$) and 871.4 eV (Ni $2p_{1/2}$) are assigned to the binding energy of Ni–O species, accompanied by two satellite bands, respectively.[39] This result indicates that Ni ions have already complexed with DHTA ligands and the presence of the Ni element in the form of a divalent state. Similarly, the EDS elemental mapping of Ni-MOF-74 ultrathin nanosheets exhibits a uniform distribution of nickel and oxygen in the layered structure. Thus, all of the above-mentioned characterization results in this study confirm the formation of Ni-MOF-74 with two-dimensionalization.

Electrochemical performance of Ni-MOF-74 ultrathin nanosheets for ORR was evaluated using a standard three electrode in O_2-saturated 0.1 M KOH. In this study, a modified glassy carbon electrode (GCE) with as-prepared Ni-MOF-74 nanosheets and graphite rod were used as the working electrode and counter electrode, respectively. In order to investigate the function of the two-dimensionalization of Ni-MOF-74 for ORR, cyclic voltammetry (CV) tests of bulk and nanosheets of Ni-MOF-74 were first carried out. As shown in Fig. S5–S8,†

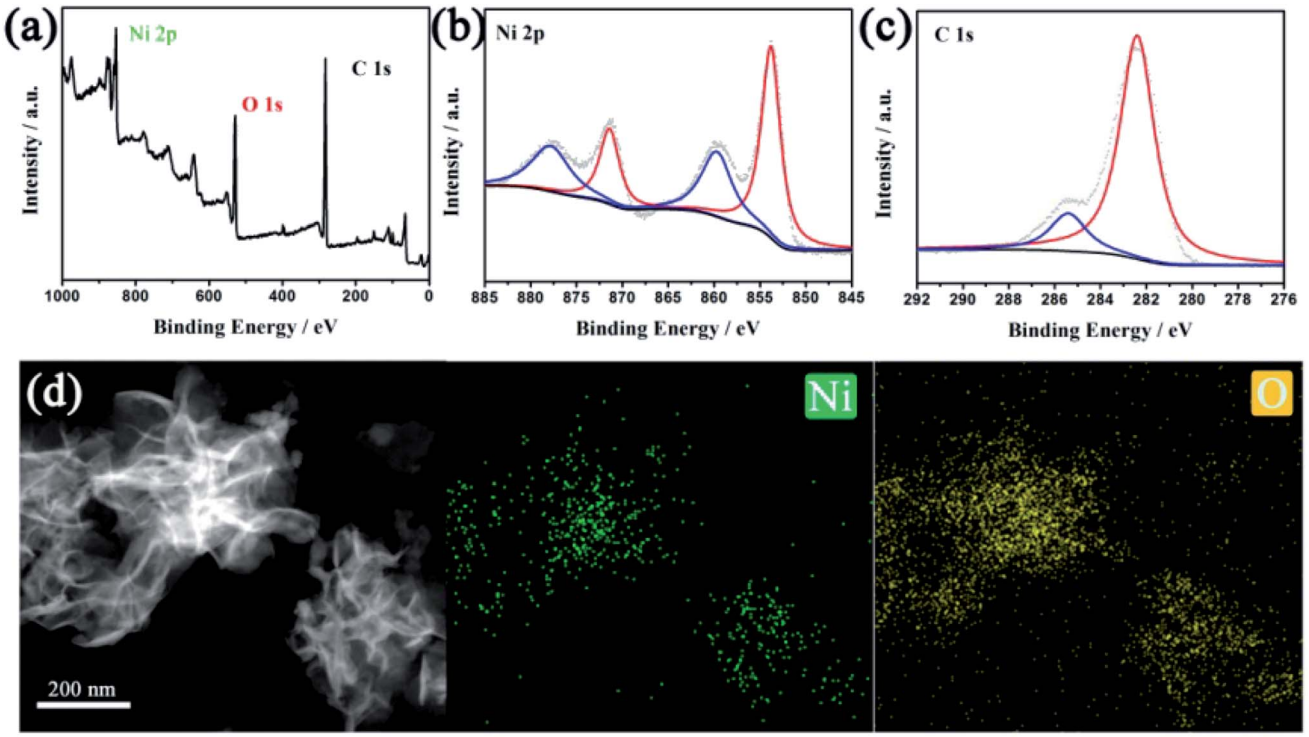

Fig. 3 (a) XPS spectrum, (b) Ni 2p high-resolution XPS and (c) 1s high-resolution XPS of Ni-MOF-74 nanosheets. (d) Mapping analysis for Ni-MOF-74 nanosheets.

compared to the oxygen-free surrounding (N_2-saturated 0.1 M KOH), the two samples both exhibit apparent oxygen reduction current, illustrating the bulk and nanosheets samples of Ni-MOF-74 exhibit electrocatalytic activities towards ORR. In Fig. 4a, the polarization curves were determined by linear sweep voltammetry (LSV) tests at a scan rate of 5 mV s^{-1} under 1600 rpm. The bulk sample exhibits a very poor activity towards ORR with negative onset (+0.77 V *vs.* RHE) and half-wave potentials (+0.64 V *vs.* RHE). The polarization curve of Ni-MOF-74 nanosheets shows a better electrocatalytic performance than that of the bulk sample. The negative onset and half-wave potentials display obviously positive shift, which are respectively located at +0.87 and +0.78 V (*vs.* RHE). Compared to the bulk sample, the ORR current density of Ni-MOF-74 nanosheets has also obviously increased. Although the two-dimensional structure can effectively enhance the electrocatalytic abilities of Ni-MOF-74 for ORR, the unsatisfied conductivity of Ni-MOF-74 leads a low capacity of electron transfer, which barely makes use of the advantages of a two-dimensional structure, limiting the subsequent ORR catalytic reaction of the Ni active center on the surface of Ni-MOF-74 nanosheets. To solve the issue, a conductive substrate (acetylene black, AB) was added into the Ni-MOF-74 nanosheets to improve its capacity of transfer electron, which could be benefit the electrocatalytic properties of Ni-MOF-74 nanosheets for ORR. In addition, AB will effectively prevent the restacking of Ni-MOF-74 nanosheets in the ORR electrocatalytic process to protect exposed nickel active centers, leading to a better electrochemical stability for Ni-MOF-74 nanosheets. Therefore, Ni-MOF-74 nanosheets with AB were prepared, denoted as Ni-MOF-74/AB. Electrochemical impedance spectra (EIS) were recorded to investigate the effects of AB for the conductivity of Ni-MOF-74 nanosheets. In Fig. S9,† the Ni-MOF-74 nanosheets without AB have a low conductivity (9324.1 Ω), while the R_{ct} of Ni-MOF-74/AB sample is getting much smaller (122.5 Ω), indicating that the existence of AB could effectively improve the ability of charge transfer for Co-PBs nanosheets. Moreover, the electrocatalytic performances of Ni-MOF-74 with AB also exhibit significant improvement for ORR. The Ni-MOF-74/AB sample possesses the most positive onset potential (+0.95 V *vs.* RHE) and half-wave potential (+0.83 V *vs.* RHE), which respectively positive shifts 176 mV and 192 mV to that of the bulk form, even close to that of the commercial Pt/C catalyst (0.98 V and 0.84 V *vs.* RHE). The electroactivity of Ni-MOF-74 nanosheets is obviously superior to the reported MOF-based electrocatalysts for ORR (Table 1). Moreover, the electrocatalytic current density (3.90 mA cm^{-2}) of the Ni-MOF-74/AB sample for ORR exhibits a significant enhancement, which is almost three times as much as that of the bulk sample (1.28 mA cm^{-2}) and comparable to that of commercial Pt/C (5.08 mA cm^{-2}). The results indicate two-dimensionalization could enhance the catalytic activities of Ni-MOF-74 for ORR and improvement of conductivity can more effectively utilize the two-dimensional structure of Ni-MOF-74 for ORR electrocatalysis.

In order to understand the electrocatalytic mechanism of Ni-MOF-74 nanosheets in the ORR process, the electron-transfer number (n) of numerous Ni-MOF-74 samples and commercial Pt/C catalyst is calculated by Koutecky–Levich (K–L) plots *via* the

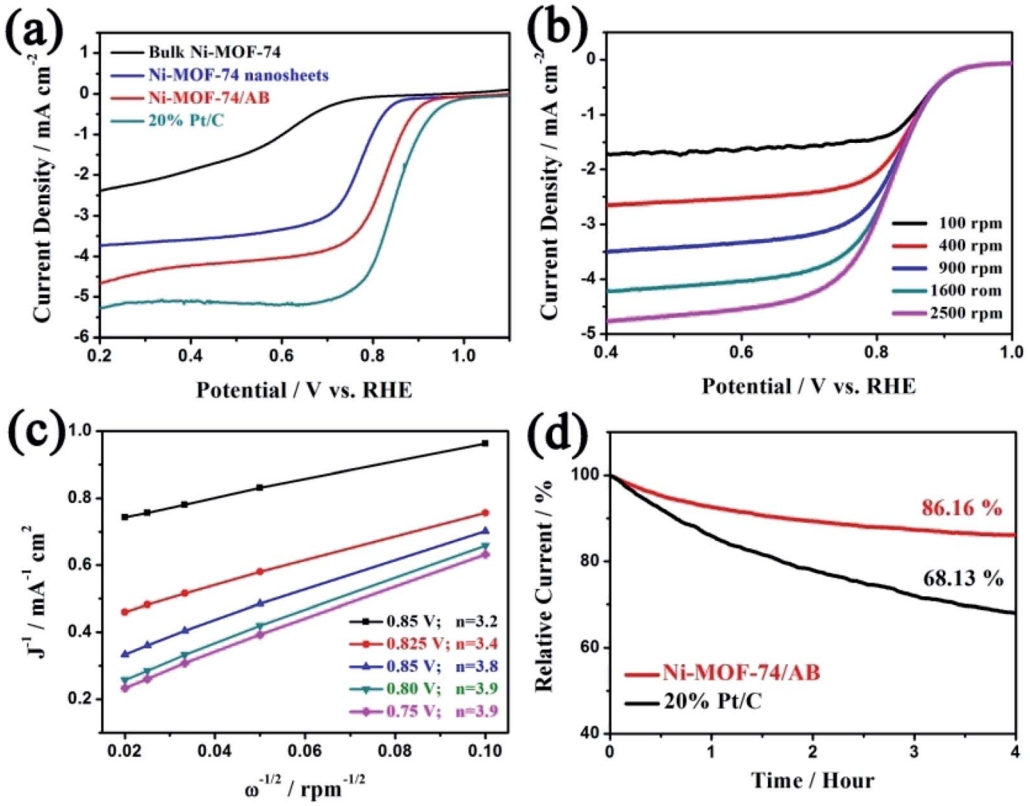

Fig. 4 (a) LSV curves of numerous Ni-MOF-74 samples and 20% Pt/C catalysts for ORR. (b) Currents of the Ni-MOF-74/AB sample with different rotating speeds. (c) The Koutecky–Levich plots of the Ni-MOF-74/AB sample. (d) The long-term durability of the Ni-MOF-74/AB-1 sample at +0.8 V (*vs.* RHE).

Table 1 The ORR activity comparison of MOF-74 nanosheets with other MOFs electrocatalysts

Sample	Electrolyte	Half-wave potential	*n*	Ref.
MOF-74 nanosheets	0.1 M KOH	+0.83 V *vs.* RHE	3.90	This work
Mil-1000	0.1 M KOH	+0.57 V *vs.* RHE	2.75	40
ZiF-1000	0.1 M KOH	+0.80 V *vs.* RHE	3.87	40
HCF-MOF-3	0.1 M KOH	+0.82 V *vs.* RHE	~4	41
ZIF-7	0.1 M KOH	+0.70 V *vs.* RHE	3.68	42
ZIF-67	0.1 M KOH	+0.71 V *vs.* RHE	3.7	43
Co-ZIF-8	0.1 M KOH	+0.71 V *vs.* RHE	3.5	44
Fe-ZIF-8	0.1 M KOH	+0.73 V *vs.* RHE	3.98	45

LSV curves at different rotation speeds of RDE. Owing to the shortened diffusion layer, the current density will enhance with the increase in the rotation rate, as shown in Fig. 4b. The corresponding K–L plots at different electrode potentials in Fig. 4c exhibits a good relationship of linearity. The Ni-MOF-74/AB sample possesses a higher catalytic efficiency (n = 3.9) in all Ni-MOF-74 samples, indicating that the electrocatalytic product of this process is water, which is similar to that of the Pt/C catalyst (Fig. S10†). The result illustrates that two-dimensionalization can obviously enhance the efficiency of Ni-MOF-74 for the ORR electrocatalytic process. On the other hand, catalytic durability is another key parameter to evaluate the property of catalysts. In Fig. 4d, the stabilities of the Ni-MOF-74/AB sample and the 20% Pt/C catalyst were tested *via* the chronopotentiometry measurement for ORR. Through a catalytic process of 4 h at +0.80 V (*vs.* RHE), the Ni-MOF-74/AB sample still maintains major catalytic current, and the attenuation of current is only 13.84%, which is lower than that of 20% Pt/C catalyst (30.87%). The preferable electrocatalytic stability of the Ni-MOF-74/AB sample may be attributed to its unique 3D porous structure and carbon substrate (AB), which could prevent the re-aggregation of Ni-MOF-74 in the ORR catalytic process to retain high catalytic activity. Therefore, the as-prepared Ni-MOF-74 ultrathin nanosheets exhibit excellent electrocatalytic performance for ORR with a positive half-wave potential, good four-electron selectivity and promising long-

term durability, which could be a promising candidate for effective energy conversion systems (fuel cells and metal–air batteries).

4. Conclusion

In summary, the two-dimensionalization of Ni-MOF-74 is achieved by using the LDH layered template, which effectively restrains the vertical growth of Ni-MOF-74 *via* the effects of steric hindrance. Owing to the extra exposed active centers and better electron-transfer ability, the two-dimensional structure endows Ni-MOF-74 with an enhanced electrocatalytic property for ORR. As a result, Ni-MOF-74/AB displays the best ORR catalytic performance with positive half-wave potential (+0.83 V *vs.* RHE), a large current density (3.9 mA cm^{-2}), four-electron selectivity (n = 3.9) and a promising long-term durability. Thus, Ni-MOF-74 nanosheets could be a promising electrocatalyst for the energy conversion systems of fuel cells and metal–air batteries. Furthermore, it is expected that our finding could contribute to the expansion of the application of MOF materials in renewable energy conversion systems.

Conflicts of interest

There are no conflicts to declare.

References

1 H.-C. J. Zhou and S. Kitagawa, *Chem. Soc. Rev.*, 2014, **43**, 5415–5418.
2 H.-C. Zhou, J. R. Long and O. M. Yaghi, *Chem. Rev.*, 2012, **112**, 673–674.
3 J.-R. Li, R. J. Kuppler and H.-C. Zhou, *Chem. Soc. Rev.*, 2009, **38**, 1477–1504.
4 H. Furukawa, K. E. Cordova, M. O'Keeffe and O. M. Yaghi, *Science*, 2013, **341**, 1230444.
5 L. Ma, C. Abney and W. Lin, *Chem. Soc. Rev.*, 2009, **38**, 1248–1256.
6 S. Ma and H.-C. Zhou, *Chem. Commun.*, 2010, **46**, 44–53.
7 L. E. Kreno, K. Leong, O. K. Farha, M. Allendorf, R. P. Van Duyne and J. T. Hupp, *Chem. Rev.*, 2012, **112**, 1105–1125.
8 B. Li, H.-M. Wen, Y. Cui, W. Zhou, G. Qian and B. Chen, *Adv. Mater.*, 2016, **28**, 8819–8860.
9 Z. Hu, B. J. Deibert and J. Li, *Chem. Soc. Rev.*, 2014, **43**, 5815–5840.
10 P. Horcajada, R. Gref, T. Baati, P. K. Allan, G. Maurin, P. Couvreur, G. Férey, R. E. Morris and C. Serre, *Chem. Rev.*, 2012, **112**, 1232–1268.
11 X. Zheng, Y. Cao, D. Liu, M. Cai, J. Ding, X. Liu, J. Wang, W. Hu and C. Zhong, *ACS Appl. Mater. Interfaces*, 2019, **11**, 15662–15669.
12 H. Yoon, S. Lee, S. Oh, H. Park, S. Choi and M. Oh, *Small*, 2019, **15**, 1805232.
13 H. Zhang, H. Osgood, X. Xie, Y. Shao and G. Wu, *Nano Energy*, 2017, **31**, 331–350.
14 Y. Shi, A.-F. Yang, C.-S. Cao and B. Zhao, *Coord. Chem. Rev.*, 2019, **390**, 50–75.
15 F. Zheng, D. Xiang, P. Li, Z. Zhang, C. Du, Z. Zhuang, X. Li and W. Chen, *ACS Sustainable Chem. Eng.*, 2019, **7**, 9743–9749.
16 T. Liu, P. Li, N. Yao, T. Kong, G. Cheng, S. Chen and W. Luo, *Adv. Mater.*, 2019, **31**, 1806672.
17 Q.-G. Zhai, X. Bu, X. Zhao, D.-S. Li and P. Feng, *Acc. Chem. Res.*, 2017, **50**, 407–417.
18 L. Jiao, Y. Wang, H. L. Jiang and Q. Xu, *Adv. Mater.*, 2018, **30**, 1703663.
19 M. Zhao, Q. Lu, Q. Ma and H. Zhang, *Small Methods*, 2017, **1**, 1600030.
20 Y. Sun, Z. Sun, S. Gao, H. Cheng, Q. Liu, J. Piao, T. Yao, C. Wu, S. Hu, S. Wei and Y. Xie, *Nat. Commun.*, 2012, **3**, 1057.
21 F. Wang, Y. Li, T. A. Shifa, K. Liu, F. Wang, Z. Wang, P. Xu, Q. Wang and J. He, *Angew. Chem., Int. Ed.*, 2016, **55**, 6919–6924.
22 Y. Sun, F. Lei, S. Gao, B. Pan, J. Zhou and Y. Xie, *Angew. Chem., Int. Ed.*, 2013, **52**, 10569–10572.
23 F. Wang, Z. X. Wang, T. A. Shifa, Y. Wen, F. M. Wang, X. Y. Zhan, Q. S. Wang, K. Xu, Y. Huang, L. Yin, C. Jiang and J. He, *Adv. Funct. Mater.*, 2017, **27**, 1603254.
24 L. Huang, X. Zhang, Y. Han, Q. Wang, Y. Fang and S. Dong, *J. Mater. Chem. A*, 2017, **5**, 18610–18617.
25 J. Duan, S. Chen and C. Zhao, *Nat. Commun.*, 2017, **8**, 15341.
26 B. Tan, H. Zhao, W. Wu, X. Liu, Y. Zhang and X. Quan, *Nanoscale*, 2017, **9**, 18699–18710.
27 N. L. Rosi, J. Kim, M. Eddaoudi, B. L. Chen, M. O'Keeffe and O. M. Yaghi, *J. Am. Chem. Soc.*, 2005, **127**, 1504–1518.
28 T. Xiao and D. Liu, *Microporous Mesoporous Mater.*, 2019, **283**, 88–103.
29 E. D. Bloch, L. J. Murray, W. L. Queen, S. Chavan, S. N. Maximoff, J. P. Bigi, R. Krishna, V. K. Peterson, F. Grandjean, G. J. Long, B. Smit, S. Bordiga, C. M. Brown and J. R. Long, *J. Am. Chem. Soc.*, 2011, **133**, 14814–14822.
30 N. Nijem, J.-F. Veyan, L. Kong, H. Wu, Y. Zhao, J. Li, D. C. Langreth and Y. J. Chabal, *J. Am. Chem. Soc.*, 2010, **132**, 14834–14848.
31 A. R. Millward and O. M. Yaghi, *J. Am. Chem. Soc.*, 2005, **127**, 17998–17999.
32 D.-A. Yang, H.-Y. Cho, J. Kim, S.-T. Yang and W.-S. Ahn, *Energy Environ. Sci.*, 2012, **5**, 6465–6473.
33 L. Yan, L. Cao, P. Dai, X. Gu, D. Liu, L. Li, Y. Wang and X. Zhao, *Adv. Funct. Mater.*, 2017, **27**, 1703455.
34 L. Ye, G. Chai and Z. Wen, *Adv. Funct. Mater.*, 2017, **27**, 1606190.
35 W. T. Reichle, *J. Catal.*, 1985, **94**, 547–557.
36 W. Shi, S. He, M. Wei, D. G. Evans and X. Duan, *Adv. Funct. Mater.*, 2010, **20**, 3856–3863.
37 M. Zhao, Y. Huang, Y. Peng, Z. Huang, Q. Ma and H. Zhang, *Chem. Soc. Rev.*, 2018, **47**, 6267–6295.
38 J. Shah, T. Wu, J. Lucero, M. A. Carreon and M. L. Carreon, *ACS Sustainable Chem. Eng.*, 2019, **7**, 377–383.
39 Z. Gao, Z. W. Yu, F. Q. Liu, Y. Yu, X. M. Su, L. Wang, Z. Z. Xu, Y. L. Yang, G. R. Wu, X. F. Feng and F. Luo, *Inorg. Chem.*, 2019, **58**, 11500–11507.

40 H. Wang, F. X. Yin, N. Liu, R. H. Kou, X. B. He, C. J. Sun, B. H. Chen, D. J. Liu and H. Q. Yin, *Adv. Funct. Mater.*, 2019, **29**, 1901531.
41 W. Li, C. Wu, H. Ren, W. Fang, L. Zhao and K. N. Dinh, *Batteries Supercaps*, 2020, **3**, 1321–1328.
42 P. Zhang, F. Sun, Z. Xiang, Z. Shen, J. Yun and D. Cao, *Energy Environ. Sci.*, 2014, **7**, 442–450.
43 M. Liu, Y. Song, S. He, W. W. Tjiu, J. Pan, Y.-Y. Xia and T. Liu, *ACS Appl. Mater. Interfaces*, 2014, **6**, 4214–4222.
44 J. Wei, Y. Hu, Y. Liang, B. Kong, J. Zhang, J. Song, Q. Bao, G. P. Simon, S. P. Jiang and H. Wang, *Adv. Funct. Mater.*, 2015, **25**, 5768–5777.
45 Q. Lai, L. Zheng, Y. Liang, J. He, J. Zhao and J. Chen, *ACS Catal.*, 2017, **7**, 1655–1663.